DE GRUYTER Nanotechnol Rev 2017; 6(6): 505–516

Hongguang Yu, Chenglin Chu* and Paul K. Chu

Self-assembly and enhanced visible-light-driven photocatalytic activity of reduced graphene oxide-Bi_2WO_6 photocatalysts

https://doi.org/10.1515/ntrev-2017-0153
Received June 16, 2017; accepted August 2, 2017; previously published online September 5, 2017

Abstract: The reduced graphene oxide-Bi_2WO_6 (rGO-BWO) photocatalysts with different R_M values (mass ratio of GO and Bi_2WO_6) had been successfully synthesized via hydrothermal method in the presence of GO. When increasing the R_M values from 0 to 2%, the evident red shift of the absorption edges of rGO-BWO samples occurred, and the photocatalytic activities for the degradation of Rhodamine-B were enhanced gradually. However, there was a significant blue shift in the absorbance band, and the morphology of the incomplete rGO-BWO microspheres led to the lower photocatalytic activity when R_M is increased from 4 to 10%. The enhanced photocatalytic activity can be attributed to the smaller band gap, which means needing less energy for the electron transition, the morphology of the unbroken microsphere that provides more possible reaction sites for the photocatalytic reaction, the appropriate GO content that may effectively mitigate electron-hole pair recombination by the migration of photoinduced electrons.

Keywords: Bi_2WO_6; hydrothermal method; photocatalytic activity; rGO-BWO.

1 Introduction

In the recent years, the researchers are giving more and more attention to solving the various widespread pollution of effluents from urban and agricultural industries including biorecalcitrant and organic pollutants [1]. Various catalytic materials have been researched in environmental protection, especially photodegradation photocatalysts. They have attracted increasing interest in environmental applications such as air purification [2–4], water disinfection [5, 6], hazardous waste degradation [7, 8], as well as sewage treatment and purification [9, 10]. Because of good chemical stability, high oxidized activity, visible light excitation, and low price, Bi_2WO_6 (BWO) has been the popular photocatalyst for environmental purification [11–20].

However, the band gap of BWO is large, and it can only be excited by a small fraction of visible light. Furthermore, rapid recombination of the photogenerated electron-hole pairs in BWO is responsible for the low efficiency of solar energy utilization hampering application of BWO [1]. Therefore, the smaller band gap and the suppression of recombination of electron-hole pairs are the key for the improvement of photocatalytic activity. Efforts have been made to modify BWO-based photocatalysts by doping with metals or non-metals, co-doping with two or more species, and coupling with metals or graphene [20–28]. Among the various approaches, graphene oxide (GO)-BWO hybrid materials have recently attracted a lot of attention because combining GO and BWO can potentially mitigate electron-hole pair recombination. GO is composed of graphite nanosheets with oxygen-containing functional groups such as hydroxyl, epoxide groups, and carboxyl groups covalently bonded to the edge of the nanosheets [29, 30]. These oxygen-containing functional groups allow transmission of cations and provide reactive sites for nucleation and growth of the nanoplates. In addition, the incorporation of reduced graphene oxide (rGO) nanosheets into BWO benefits the transfer and separation of photogenerated carriers because conversion of GO to rGO suppresses charge recombination effectively [1]. Although there are many methods for the preparation of graphene-based hybrids, they just mix rGO and BWO together and, thus, limit the advantages of rGO into full play. Most of the BWO-graphene composites have been fabricated *in situ* [23, 31–35], and the growth of BWO nanoplates on the layered graphene nanosheets can be hampered. On the other hand, there are very few studies

---

***Corresponding author: Chenglin Chu,** School of Materials Science and Engineering, Southeast University, Nanjing 211189, China; and Jiangsu Key Laboratory for Advanced Metallic Materials, Southeast University, Nanjing 211189, China, e-mail: clchu@seu.edu.cn
Hongguang Yu: School of Materials Science and Engineering, Southeast University, Nanjing 211189, China; and Jiangsu Key Laboratory for Advanced Metallic Materials, Southeast University, Nanjing 211189, China
Paul K. Chu: Department of Physics and Materials Science, City University of Hong Kong, Tat Chee Avenue, Kowloon, Hong Kong, China

that focus on an alternative method by controlling the morphology of rGO-BWO to improve the photocatalytic properties. It is possible to integrate the advantages of the 3D morphology of BWO microspheres and the ability of separation and transport of photocarriers of rGO into a composite leading to improving the photocatalytic properties.

In this study, the visible-light-driven rGO-BWO samples with different R_M values (mass ratio of GO and Bi_2WO_6) are synthesized successfully by a facile hydrothermal method, and the photocatalytic activity is evaluated. Introduction of rGO into BWO affects not only the band gap, but also the photocatalytic activity because the rGO nanosheets serving as charge transfer channels on BWO attract electrons to mitigate charge pair recombination under visible light irradiation, and the effectiveness is investigated based on the degradation of Rhodamine-B (RhB) [27]. Our research provides a facile method to enhance the visible-light-driven photocatalytic activity by introducing rGO into photocatalysts and may be further extend to the mentality of designing highly efficient visible-light-driven semiconductors for environmental remediation.

2 Experimental details

2.1 Synthesis of graphene oxide (GO) samples

GO was synthesized from the oxidation of graphite by the modified Hummers method. The method involved three steps: oxidation, purification and exfoliation. Two grams of graphite and 1 g of $NaNO_3$ were added to a three-neck round-bottomed flask containing 46 ml of concentrated sulfuric acid and put in an ice bath under stirring. Six grams of $KMnO_4$ powders was added slowly to the above-mentioned flask, and the color of the mixed solution turned green gradually. After magnetic stirring for 1 h, the mixed solution was heated to 35°C, with heat preservation for 0.5 h. Subsequently, 92 ml of deionized water was added dropwise, and the color of the solution changed from brown to bright yellow. The solution was heated to 98°C and was maintained for 30 min. Finally, the reaction was terminated by the addition of 280 ml of H_2O and 6 ml of 30% H_2O_2. After a standing time of the synthetic samples for 2 h, the products were centrifuged and washed several times with deionized water to get rid of SO_4^{2-}, and GO was obtained after freeze drying under vacuum.

2.2 Preparation of graphene-Bi_2WO_6 (rGO-BWO)

All the chemicals were of analytical grade and used without further purification. Deionized water was used throughout the experimental process. GO powders with different R_M values were mixed with a 50-ml aqueous solution containing 2 mmol of citric acid (R_M is the mass ratio of GO and Bi_2WO_6 sample, R_M = 2‰, 4‰, 6‰, 8‰, 1%, 2%, 4%, 6%, 8%, 10%, respectively). After magnetic stirring for 30 min, 2 mmol of $Bi(NO_3)_3 \cdot 5H_2O$ was added into the above-mentioned mixed solution. After stirring for 1 h, 1 mmol of $Na_2WO_4 \cdot 2H_2O$ and 4 mmol of $NaHCO_3$ were added gradually and sufficiently stirred for another 1 h. Afterward, the suspension was transferred to a stainless steel autoclave with a 100-ml Teflon liner and heated at 200°C for 24 h. After the autoclave cooled to room temperature, the products were separated centrifugally and washed three times with deionized water and absolute ethanol, respectively. Finally, the products were obtained by drying under vacuum at 60°C for 20 h.

2.3 Characterization

The crystal structure of the samples was characterized by X-ray diffraction (XRD) (Bruker D8-Discover XRD, Germany) with Cu K_α radiation (λ = 1.54 Å) in the 2θ range of 5°–70°. Field-emission environmental scanning electron microscopy (FEESEM) was carried out on a FEI 3D scanning electron microscope (USA). Transmission electron microscopy (TEM) and selected-area electron diffraction (SAED) were performed with the G2 20 high-resolution TEM (FEI, USA) at an accelerating voltage of 200 kV. The Brunauer-Emmett-Teller (BET) surface area of the samples was determined by the AUTOSORB-IQ2 nitrogen adsorption apparatus. X-ray photoelectron spectroscopy (XPS) analysis was employed on the Physical Electronics PHI 5802 X-ray photoelectron spectrometer (VG Scientific, UK) using a Mg Kα radiation source. The optical diffuse reflectance spectra were recorded on a Japan Shimadzu UV-2550 (Japan) using $BaSO_4$ as the reference. Photoluminescence (PL) spectra were carried out with a Hitachi F-4600 fluorescence spectrophotometer at room temperature.

2.4 Photocatalytic assessment

The photocatalytic activity of the rGO-BWO samples was evaluated based on the degradation of RhB under 500-W Xe light irradiation. Of the photocatalyst, 0.1 g was added to each test tube containing 30 ml of the RhB solution (5 mg/l). Before illumination, the suspensions were magnetically stirred in darkness for 1 h to ensure the establishment of the adsorption-desorption equilibrium between the photocatalysts and RhB. Subsequently, the solution was irradiated with 500-W Xe light under magnetic stirring. At given intervals of 20 min, one test tube was sampled and centrifuged to remove the photocatalysts. The supernatant was analyzed by monitoring the variation in the absorption band maximum (553 nm) in the UV-vis spectra of RhB using a Shimadzu UV-2550 spectrophotometer (Japan).

3 Results and discussion

3.1 Structure and morphology

The XRD patterns of BWO and rGO-BWO microspheres are presented in Figure 1. As shown in Supplementary Figure 1A and B, the diffraction peak of GO at about 11° corresponds to the layer-to-layer distance of 0.82 nm. As there is only one peak in the XRD pattern of GO, and the other characteristic peaks of graphite cannot be detected, highly oxidized GO samples are obtained as reported in the related literature [36]. In comparison with the XRD patterns of GO, the disappearance of strong diffraction peaks from all the as-prepared composites suggests a conversion of GO to reduced graphene oxide and may be attributed to the small weight content and weak diffraction intensity of GO [37–40]. As shown in Figure 1, the as-prepared samples show characteristic peaks corresponding to the (113), (200), (220), and (313) planes of the orthorhombic Bi_2WO_6 (JCPD file No. 73-2020). The main diffraction peaks and the full width at half maximum (FWHM) of BWO and rGO-BWO samples with different R_M values are similar to that of pure BWO, demonstrating that the introduction of rGO has little effects on the crystalline size of BWO in the rGO-BWO nanocomposites as well as on the preferential orientation. However, with the increasing R_M values (Figure 1C and D), comparison of the (113) diffraction peaks in the range of $2\theta = 27$–$30°$ shows that the peak position of rGO-BWO shifts slightly toward the larger 2θ as reported in the literature [41]. According to Bragg's law, the increase in 2θ should result in a decrease in the

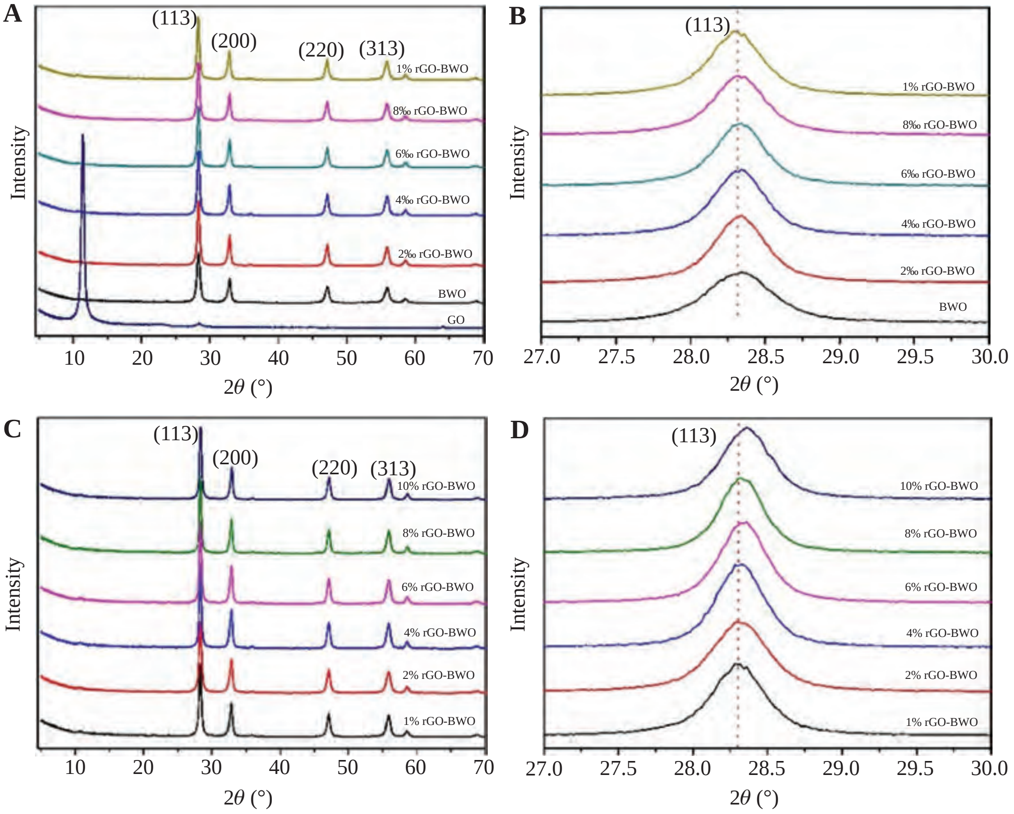

Figure 1: XRD patterns of the as-synthesized GO and rGO-BWO samples with different R_M values: (A) GO, BWO ($R_M = 0$), $R_M = 2‰$, 4‰, 6‰, 8‰, 1%; (B) magnified XRD patterns in 27°–30°; (C) $R_M = 1\%$, 2%, 4%, 6%, 8%, 10%; (D) magnified XRD patterns in 27°–30°.

lattice parameters [*d*(113) value]. The oxygen-containing functional groups attached on both sides of the graphene nanosheets make the lattice structure of BWO closer because of the interaction of the oxygen-containing functional group and BWO.

Figures 2 and 3 depict the FE-ESEM images of the rGO-BWO microspheres with different R_M values. As shown in Figures 2 and 3, the low-magnification images reveal that all the products are composed of many microspheres, which are regular in shape and uniform in size, and the higher-magnification FEESEM images show that the as-synthesized samples are composed of numerous square nanoplates. As the rGO content goes up, the morphology and structure of the rGO-BWO microspheres with different R_M values are maintained, and no change almost can be observed by comparing Figures 2A and 3F, suggesting that a moderate rGO content has little influence on the formation of rGO-BWO microspheres, and the process of the preparation of the microspheres is reasonable. The rGO-BWO microspheres with different R_M values are expected to have better photocatalytic properties because of high crystallinity and good morphology, that is to say, fewer traps, larger specific surface area, and stronger photocatalytic activity [11]. Obvious morphological changes are observed for $R_M = 8–10\%$ due to the effect of rGO as the reaction activation center in the growth of the nanoplates. On account of the large number of functional groups on the surface of graphene, the tendency of nanoplate accumulation in the microspheres is altered resulting in random aggregation of nanoplates. The results indicate that an excessive amount of rGO compromises the formation of rGO-BWO microspheres.

As shown in Figure 4, TEM is employed to understand the detailed morphological and structural characteristics of the as-synthesized samples. Figure 4A–C displays the TEM images of the membrane-like GO nanosheets on the copper grid with overlapping layers and a wrinkled surface texture. The SAED pattern in the inset shows that the diffraction pattern of GO is a ring, and it reveals that the as-synthesized GO is 3~4 layers thick and

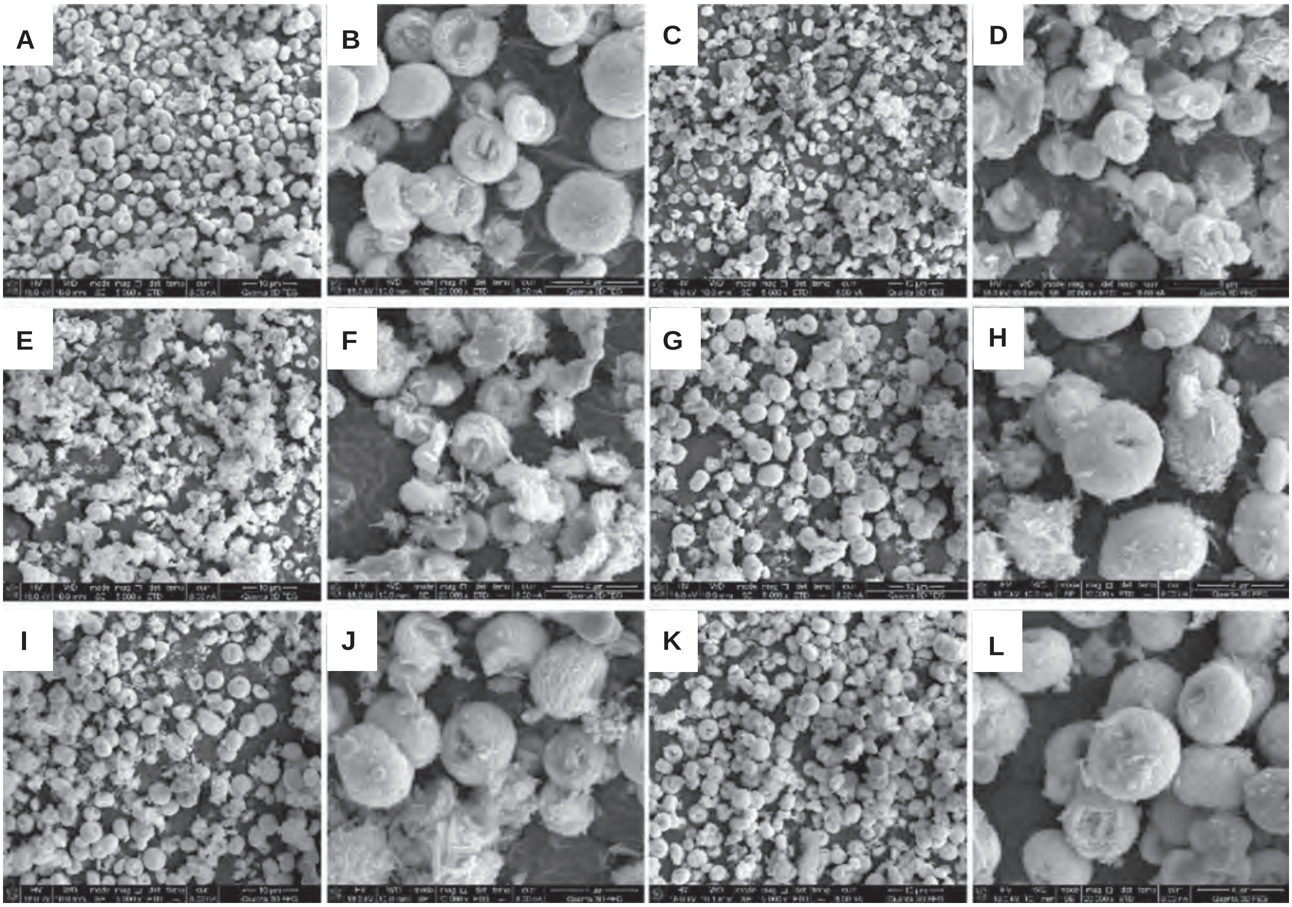

Figure 2: FE-ESEM images of rGO-BWO samples with different R_M values: (A) BWO; (C) $R_M = 2‰$; (E) $R_M = 4‰$; (G) $R_M = 6‰$; (I) $R_M = 8‰$; (K) $R_M = 1\%$. (B), (D), (F), (H), (J) and (L) higher-magnification SEM image of (A), (C), (E), (G), (I) and (K), respectively.

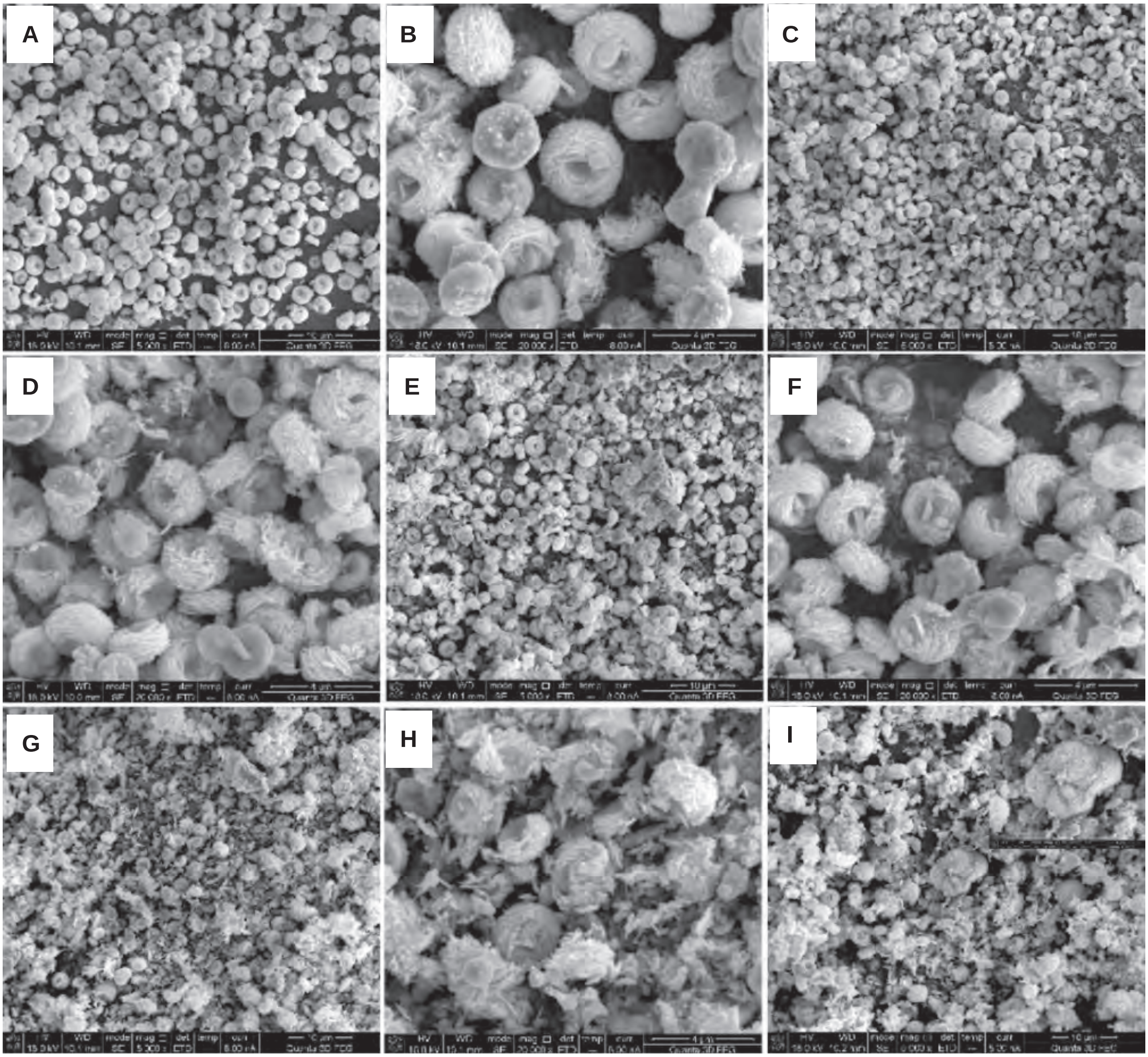

Figure 3: FE-SEM images of the rGO-BWO samples with different R_M values: (A) $R_M = 2\%$; (C) $R_M = 4\%$; (E) $R_M = 6\%$; (G) $R_M = 8\%$; (I) $R_M = 10\%$. (B), (D), (F) and (H) higher-magnification SEM image of (A), (C), (E) and (G), respectively.

demonstrates better exfoliation in Figure 4C. As shown in Figure 4D–F, the average size of the BWO microspheres is about 3 μm, and they consist of approximate square regular nanoplates. The diffraction spots of the sample is also further investigated and shows a SAED pattern at the corner of Figure 4F, which confirms that the nanoplates have a single crystal structure. Figure 4G–I reveals that the 2% rGO-BWO is similar to BWO in morphology, but a large difference is observed from the SAED pattern of BWO in Figure 4I. The diffraction pattern of the 2% rGO-BWO is no longer independent of the diffraction spot, but the diffraction ring is similar to that of GO. The results suggest that the introduction of GO affects the crystalline structure, and the graphene and BWO nanoplates are arranged layer-by-layer rather than by surface adsorption.

The oxidation states and surface chemical composition of GO, BWO, and rGO-BWO samples were characterized by X-ray photoelectron spectroscopy (XPS) as shown in Figure 5. As shown in Figure 5B, the C1s XPS spectrum of rGO-BWO had an obvious change compared to that of GO. The result also demonstrated that GO could be efficiently reduced by a hydrothermal method. As shown in Figure 5C, the spin orbit components of $Bi4f_{5/2}$ consist of a peak with binding energies at 164.6 eV, corresponding

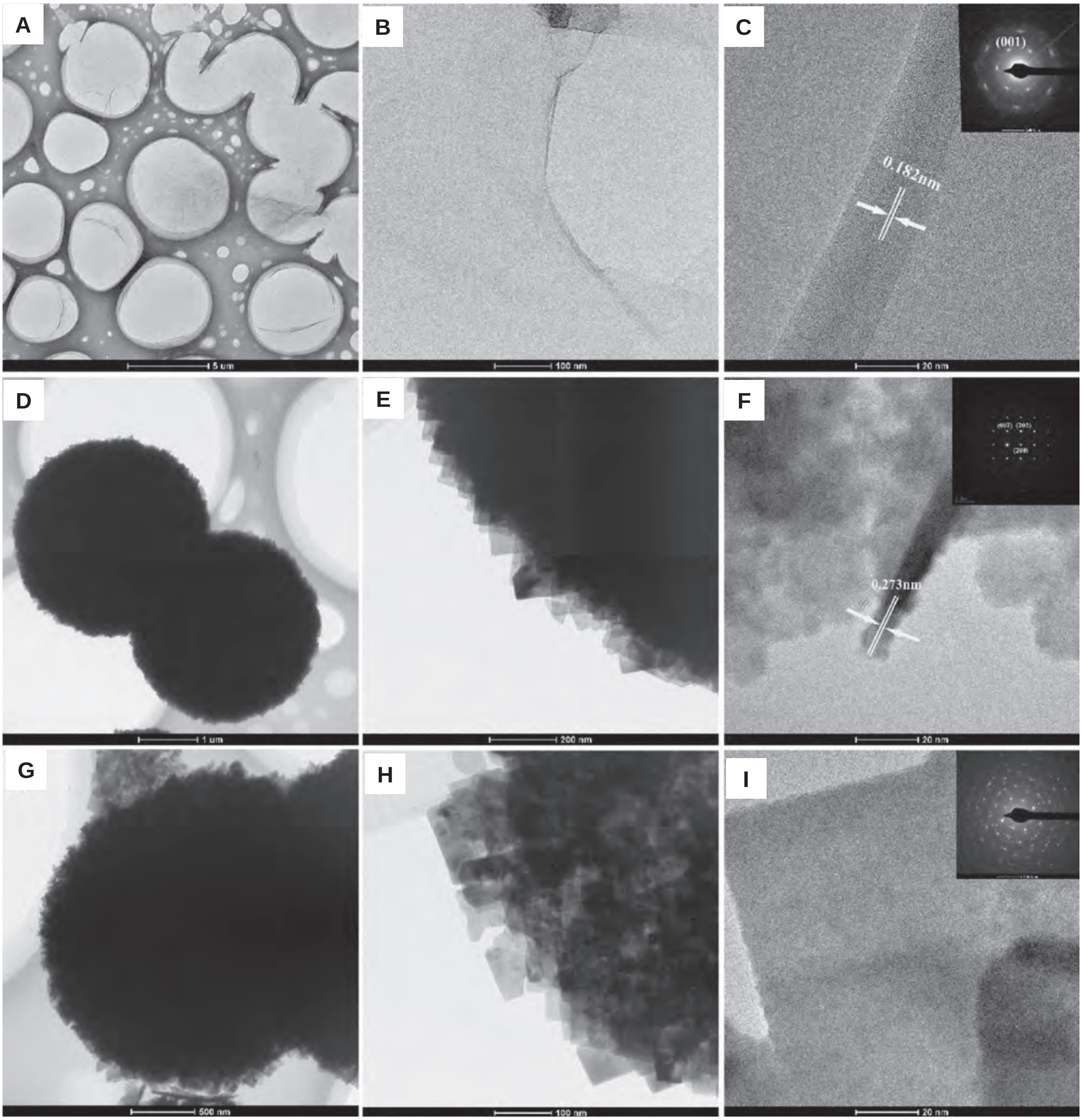

Figure 4: TEM images of the as-synthesized GO, BWO, 2% rGO-BWO samples: (A), (B) and (C) GO; (D), (E) and (F) BWO; (G), (H) and (I) 2% rGO-BWO (inset: SAED pattern).

to Bi^{3+} in the crystal structure. Meanwhile, the feature in the $Bi4f_{7/2}$ spectrum at 159.3 eV is a characteristic peak of the Bi^{3+} ions in BWO and rGO-BWO [42]. As shown in Figure 5D, the two bands at 37.8 eV and 35.6 eV are ascribed to $W4f_{5/2}$ and $W4f_{7/2}$, respectively [25, 43]. Compared to that of pure BWO, the binding energies of the Bi and W peaks of rGO-BWO almost have no change. It suggests that the coordination environment of the Bi surroundings and the WO_6 octahedron was not influenced by the introduction of GO, and it was beneficial to maintain the morphology of the rGO-BWO microspheres.

Based on the above observations, the growth mechanism of the rGO-BWO microspheres is shown in Scheme 1. GO is dispersed evenly in the citric acid solution, and Bi^{3+} adsorbs onto the oxygen-containing functional groups of GO when $Bi(NO_3)_3 \cdot 5H_2O$ is added to the solution. After

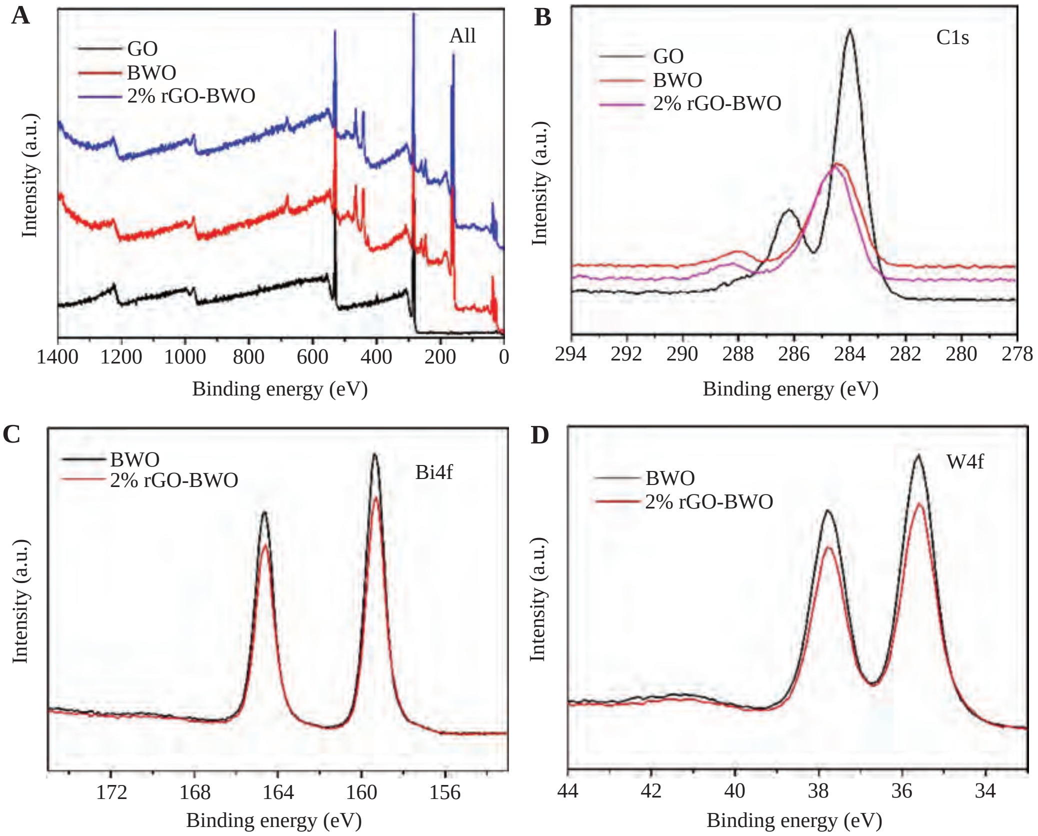

Figure 5: XPS spectra of GO, BWO and rGO-BWO samples: (A) survey, (B) C1s, (C) Bi4f, (D) W4f.

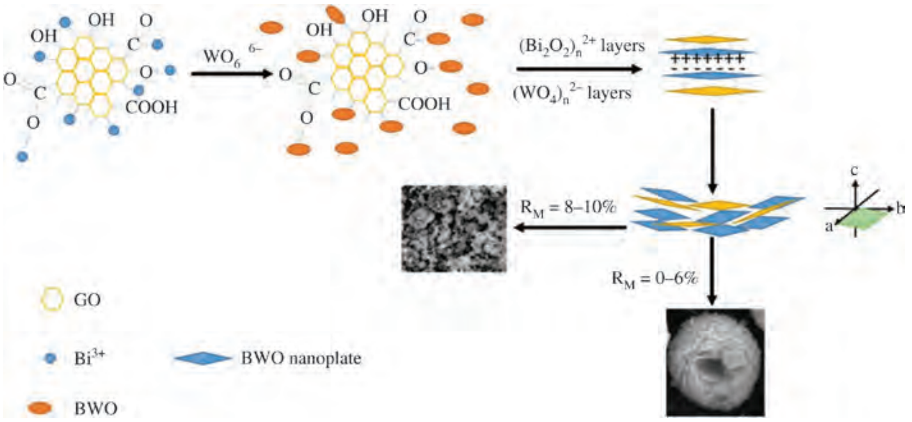

Scheme 1: Formation mechanism of the rGO-BWO microspheres.

$Na_2WO_4 \cdot 2H_2O$ and $NaHCO_3$ are added, WO_4^{2-} combines with Bi-GO to form GO-BWO and/or BWO nanoparticles. Meanwhile, the GO nanoplates selectively adsorb onto the newly formed BWO nanoparticles to suppress the intrinsic anisotropic growth [44]. The positive $(Bi_2O_2)_n^{2+}$ layers and negative $(WO_4)_n^{2-}$ layers of the orthorhombic BWO is stacked along the c axis, and the GO-BWO and/or BWO nanoplates stack or connect to the BWO nanoplates or GO nanoplates due to electrostatic effects of the polar charges [41]. GO is reduced to rGO, and the nanoplates stack further together in the hydrothermal process. As shown in Scheme 1, it can be deduced that there are two growth mechanisms along the circle direction. If the growth direction is along the c axis, unbroken microspheres are formed (e.g. $R_M = 0–6\%$); otherwise, the random nanoplate structure is produced (e.g. $R_M = 8–10\%$).

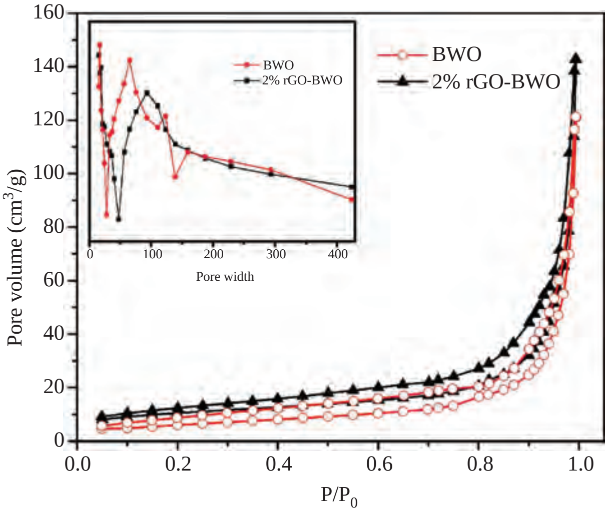

Figure 6: Nitrogen adsorption-desorption isotherms of the BWO and rGO-BWO samples. Inset: the pore size distribution curves of the BWO and rGO-BWO samples.

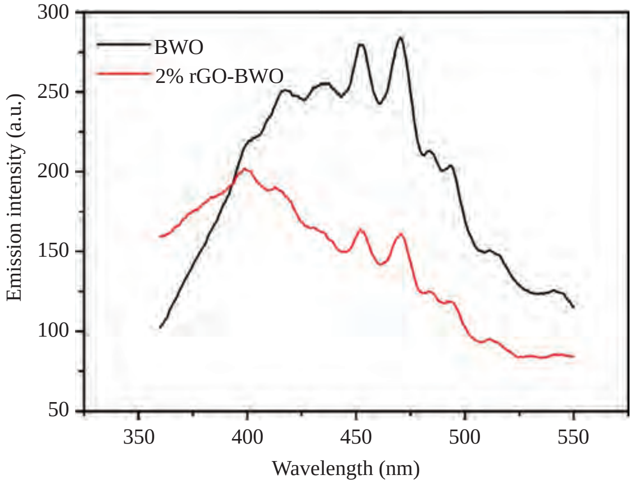

Figure 7: PL spectra of pure Bi_2WO_6, 2% rGO-BWO.

3.2 Surface analysis

The nitrogen adsorption-desorption isotherm and porosity of the sample is further investigated because the surface area is one key structural parameter for photocatalysts. As shown in Figure 6, the isothermals were categorized as type II with an H4 hysteresis loop according to the IUPAC classifications, which suggests a macroporous characteristic of rGO-BWO microspheres [45]. Moreover, the hysteresis loop of rGO-BWO shifts to left, and the BET surface area of rGO-BWO (approximately 28.148 m^2/g) is measured to be much higher than that of BWO (approximately 22.601 m^2/g), indicating that the amount of pores became more compared with that of pure BWO. As is shown in the inset of Figure 6, there was a peak concentrating at 92 nm for rGO-BWO, whereas the peak of BWO appeared at 64 nm, suggesting that the introduction of GO made between the nanosheets became bigger. The surface area is closely related to the visible light photocatalytic performance because the larger surface area can increase photo-absorption and provide more possible reaction sites for the photocatalytic reaction [46]. SorGO-BWO is reasonable to expect the excellent photocatalytic activity.

3.3 Luminescence properties of rGO-BWO

PL spectra are usually utilized to explain the separation and transfer efficiency of photon-generated carrier of the photocatalyst because PL emission mainly originates from the recombination of photon-generated holes and electrons [25]. Generally speaking, the lower PL intensity suggests a low recombination rate of photon-generated electrons and holes, and on the contrary, with higher photocatalytic activity [25, 47]. As shown in Figure 7, the emission intensity of 2% rGO-BWO is lower obviously than that of pure BWO, indicating that the introduction of GO suppresses electron-hole pair recombination by the migration of photoinduced carriers. So, the introduction of GO is beneficial to enhance the photocatalytic activity.

3.4 Optical properties of rGO-BWO

Figure 8 displays the diffuse reflectance spectra of as-synthesized BWO and rGO-BWO samples. Figure 8

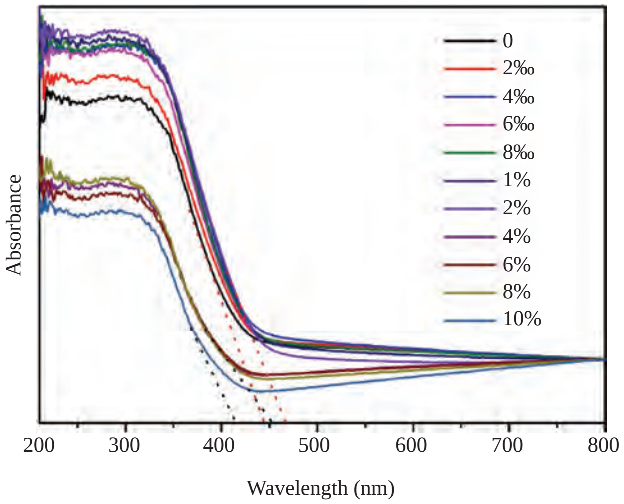

Figure 8: UV-vis diffusive reflectance spectra of the as-synthesized BWO and rGO-BWO samples.

indicates that rGO-BWO samples with different R_M values have different absorption ability for visible light when the wavelength is shorter than 470 nm. All the samples show similar absorption edges. When increasing from 0 to 2%, the absorption wavelength increases from 448 to 468 nm; in other words, the absorption wavelength is red-shift apparently. It suggests that the different absorbance edges arise from the introduction of rGO, and the band gap of rGO-BWO samples are closely related with the R_M value. However, there is a clear difference in the absorption edges by comparing the right curves, and there are significant blue-shifts when R_M is increased from 4 to 10%. The results show that the introduction of the appropriate amount of rGO enhances the absorption ability of visible light leading to red-shifts of the absorption wavelength. However, incorporation of excessive amounts of rGO can produce the opposite effects leading to blue-shifts. The results are consistent with the change in the morphology because the morphology of unbroken microspheres are beneficial to multiple scattering of the light within the microsphere. This result is consistent with the change in the morphology because the better morphology is beneficial to multiple scattering within the microsphere. This is an important factor that the absorption ability of visible light weakens when the morphology is severely damaged, especially when the R_M value is 8% or 10%. The band gap (Eg) of the rGO-BWO samples with R_M between 0 and 2% obtained by empirical equation is estimated to be 2.77 eV–2.65 eV according to the focus of the extension line of the absorption edge. The band gap is 2.75 eV–3.0 eV when R_M is changed from 4% to 10%. Generally speaking, the most appropriate band gap by considering the advantages of the graphene and BWO is 2.65 eV when R_M is 2%. It can be concluded that band gap narrowing is closely related to the introduction of rGO. First of all, introduction of rGO influences the interaction of the chemical bond between BWO and rGO resulting in an upshift of the conduction band potential and improved separation of charge carriers in the rGO-BWO nanospheres. It can be considered as generating trap energy in the band gap. Second, the degree of delocalization of the excitation energy due to the distortion of the crystal structure arises from rGO.

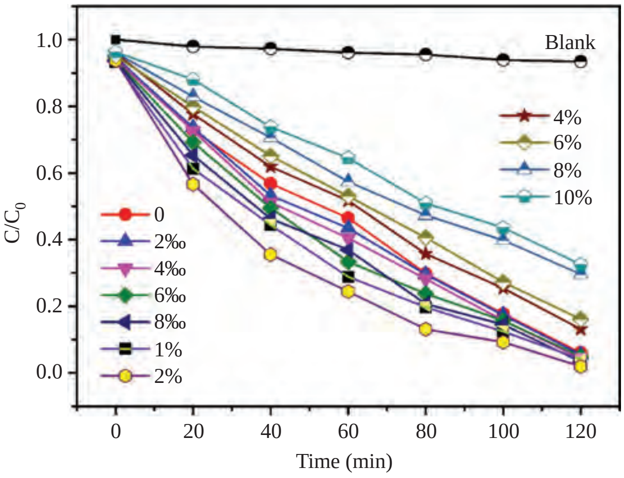

Figure 9: Photocatalytic degradation of RhB under visible light (λ > 400 nm) illumination as a function of irradiation time for the as-prepared rGO-BWO samples with different R_M values.

3.5 Photocatalytic performance of rGO-BWO

As shown in Figure 9, the photocatalytic performance of the rGO-BWO samples with different R_M values is assessed by comparing the degradation efficiency of RhB under visible light illumination (λ > 400 nm). C is the absorption of RhB after the visible light illumination, and C_0 is the absorption of RhB after the adsorption equilibrium in the ordinate in Figure 9 in which the blank test shows extremely low photodegradation efficiency without a photocatalyst and can be almost ignored. The visible-light irradiation of the aqueous RhB/rGO-BWO photocatalyst dispersions leads to different photodegradation rates of RhB, but the rGO-BWO samples have higher photocatalytic activity than pure BWO. The photoactivity is enhanced with the R_M values increasing. The highest photocatalytic performance of 95% after irradiation for 120 min is achieved for an R_M of 2%. However, the photoactivity of the rGO-BWO samples weakens when the value is 4–10%.

Our results show that the photoactivity depends on the morphology, band gap, and introduction of rGO. The morphology of the unbroken microsphere not only determines the sites for establishment of the adsorption-desorption equilibrium between the photocatalysts and RhB, but also causes multiple light scattering under the visible light illumination resulting in greater light harvesting. A smaller band gap enables easier excitation of electron-hole pairs. Introduction of rGO causes good electrical conductivity and effective charge separation, thereby, enhancing the photocatalytic activity. In the rGO-BWO samples, the electron-hole pairs are excited and generated in the valence band of BWO under visible light irradiation, and the photogenerated carriers are transferred easily to the rGO; then, the transitions of photogenerated carriers go back to the conduction band from rGO and degrade by dissolved oxygen to facilitate hole-electron separation. Meanwhile, the holes can either react with the surface hydroxyl to form hydroxyl radicals or directly oxidize various organic compounds [1]. Hence, the appropriate

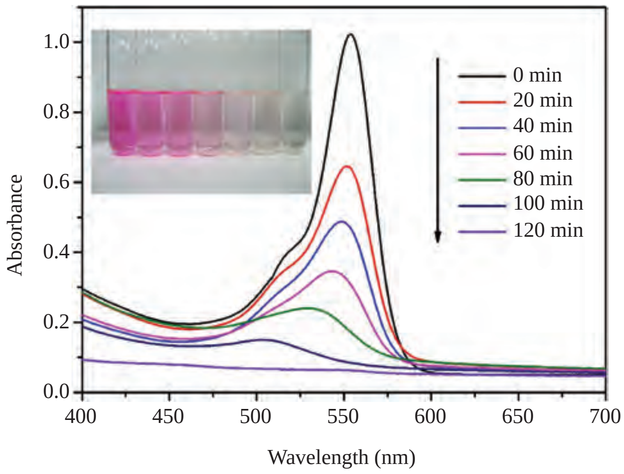

Figure 10: Temporal evolution of the absorption spectrum of the RhB solution of rGO-BWO for R_M of 2% under 500-W Xe light irradiation (inset: digital photo of the sample for a different irradiation time).

rGO content enhances the photoactivity, but the inappropriate amount reduces it.

To explain the photocatalytic activity of the photodegradation of RhB, the rGO-BWO sample with R_M value of 2% is shown as an example. Figure 10 shows the temporal evolution of the spectra at intervals of 20 min. With increasing exposure time, a sharp decrease in the absorption peak at 553 nm and the shift of the position of the absorption peak toward shorter wavelengths are observed, indicating that the de-ethylated process instead of the decomposition of the conjugated chromophore structure is the dominant mechanism [48]. The inset in Figure 10 shows the digital photo in which the test tube is irradiated for different times from left to right. After irradiation for 120 min, the absorption peak disappears almost completely, and the pink color of the RhB solution fades from pink to colorless. Meanwhile, RhB is completely decolorized on rGO-BWO.

4 Conclusion

The rGO-BWO samples with the different R_M values are synthesized hydrothermally in the presence of GO at 200°C for 24 h. With increasing contribution of rGO from $R_M = 5\%$ to 2%, the photocatalytic activity of the rGO-BWO samples that are composed of nanosheets with the orthorhombic Aurivillius layered structure is enhanced compared to pure BWO. The good electrical conductivity and effective charge separation of rGO introduced to BWO lead to red-shifts in the absorption wavelength, the larger specific surface area, and smaller band gap affecting the photocatalytic activity. All the samples degrade RhB, and rGO-BWO with an R_M of 2% shows the best photocatalytic activity under 500-W Xe light irradiation. However, the photocatalytic activity is weakened due to the incomplete morphology and wider band gap as R_M value is increased from 4 to 10%. The enhanced photocatalytic activities of rGO-BWO samples are interpreted to be the result of three factors: (1) the morphology of the unbroken microsphere can provide the greater light-harvesting capacities by multiple scattering of the light and more possible reaction sites for the photocatalytic reaction; (2) the smaller band gap reduces the electron energy from the valence band transition to the conduction band; (3) the appropriate GO content may effectively suppress electron-hole pair recombination by the migration of photoinduced carriers. Our work not only reveals feasible synthesis of the nanosheet-based rGO-BWO photocatalyst but also opens new possibilities for integrating semiconductor materials and graphene in future applications.

Acknowledgments: This work was jointly supported by the National Natural Science Foundation of China (Grant No. 31570961), the State Key Program of National Natural Science Foundation of China (Grant No. 51631003), the Fundamental Research Funds for the Central Universities and Research Innovation Program for College Graduates of Jiangsu Province (Grant No. KYLX15_0120), as well as the City University of Hong Kong Applied Research Grant (ARG) No. 9667122 and Strategic Research Grant (SRG) No. 7004644.

References

[1] Xiang QJ, Yu JG, Jaroniec M. Graphene-based semiconductor photocatalyst. *Chem. Soc. Rev.* 2012, 41, 782–796.
[2] Yu JG, Yu JC, Leung MKP, Ho W, Cheng B, Zhao XJ, Zhao J. Effects of acidic and basic hydrolysis catalysts on the photocatalytic activity and microstructures of bimodal mesoporous titania. *J. Catal.* 2003, 217, 69–78.
[3] Yu JG, Wang WG, Cheng B, Su BL. Enhancement of photocatalytic activity of mesporous TiO_2 powders by hydrothermal surface fluorination treatment. *J. Phys. Chem. C* 2009, 113, 6743–6750.
[4] Yu JG, Zhang LJ, Cheng B, Su YR. Hydrothermal preparation and photocatalytic activity of hierarchically sponge-like macro-/mesoporous titania. *J. Phys. Chem.* C 2007, 111, 10582–10589.
[5] Yu JC, Ho WK, Yu JG, Yip H, Wong PK, Zhao J. Efficient visible-light-induced photocatalytic disinfection on sulfur-doped nanocrystalline titania. *Environ. Sci. Technol.* 2005, 39, 1175–1179.
[6] Yu JG, Su YR, Cheng B. Template-free fabrication and enhanced photocatalytic activity of hierarchical macro-/mesoporous titania. *Adv. Funct. Mater.* 2007, 17, 1984–1990.

[7] Cheng B, Le Y, Yu JG. Preparation and enhanced photocatalytic activity of Ag@TiO_2 core – shell nanocomposite nanowires. *J. Hazard. Mater.* 2010, 177, 971–977.

[8] Yu JG, Dai GP, Huang BB. Fabrication and characterization of visible-light-driven plasmonic photocatalyst Ag/AgCl/TiO_2 nanotube arrays. *J. Phys. Chem.* C 2009, 113, 16394–16401.

[9] Yu JG, Xiang QJ, Ran JR, Mann S. One-step hydrothermal fabrication and photocatalytic activity of surface-fluorinated TiO_2 hollow microspheres and tabular anatase single micro-crystals with high-energy facets. *Cryst. Eng. Comm.* 2010, 12, 872–879.

[10] Xiang QJ, Yu JG, Cheng B, Ong HC. Microwave-hydrothermal preparation and visible-light photoactivity of plasmonic photocatalyst Ag-TiO_2 nanocomposite hollow spheres. *Chem.-Asian J.* 2010, 5, 1466–1474.

[11] Yu HG, Zhu ZF, Zhou JH, Wang J, Li J, Zhang Y. Self-assembly and enhanced visible-light-driven photocatalytic activities of Bi_2MoO_6 by tungsten substitution. *Appl. Surf. Sci.* 2013, 265, 424–430.

[12] Wu L, Bi JH, Li ZH, Wang X, Fu X. Rapid preparation of Bi_2WO_6 photocatalyst with nanosheet morphology via microwave-assisted solvothermal synthesis. *Catal. Today* 2008, 131, 15–20.

[13] Yu JG, Xiong JF, Cheng B, Yu Y, Wang J. Hydrothermal preparation and visible-light photocatalytic activity of Bi_2WO_6 powders. *J. Solid State Chem.* 2005, 178, 1968–1972.

[14] Li YY, Liu JP, Huang XT, Li GY. Hydrothermal synthesis of Bi_2WO_6 uniform hierarchical microspheres. *Cryst. Growth. Des.* 2007, 7, 1350–1355.

[15] Liu SW, Yu JG. Cooperative self-construction and enhanced optical absorption of nanoplates-assembled hierarchical Bi_2WO_6 flowers. *J. Solid State Chem.* 2008, 181, 1048–1055.

[16] Wang W, Yang W, Chen R, Duan X, Tian Y, Zeng D, Shan B. Investigation of band offsets of interface BiOCl:Bi_2WO_6: a first-principles study. *Phys. Chem. Chem. Phys.* 2012, 14, 2450–2454.

[17] Zhang LS, Wang HL, Chen ZG, Wong PK, Liu J. Bi_2WO_6 micro/nano-structures: synthesis, modifications and visible-light-driven photocatalytic applications. *Appl. Catal. B-Environ.* 2011, 106, 1–13.

[18] Zhang C, Zhu YF. Synthesis of square Bi_2WO_6 nanoplates as high-activity visible-light-driven photocatalysts. *Chem. Mater.* 2005, 17, 3537–3545.

[19] Cao XF, Zhang L, Chen XT, Xue ZL. Microwave-assisted solution-phase preparation of flower-like Bi_2WO_6 and its visible-light-driven photocatalytic properties. *Cryst. Eng. Comm.* 2011, 13, 306–311.

[20] Li Y, Liu J, Huang X, Yu J. Carbon-modified Bi_2WO_6 nanostructures with improved photocatalytic activity under visible light. *Dalton. Trans.* 2010, 39, 3420–3425

[21] Zhou Y, Zhang Q, Lin Y, Antonova E, Bensch W, Patzke GR. One-step hydrothermal synthesis of hierarchical Ag/Bi_2WO_6 composites: in situ growth monitoring and photocatalytic activity studies. *Sci. China. Chem.* 2013, 56, 435–442.

[22] Guo L, Wang DJ, Fu F, Qiang XD, Xu T. Synthesis of Ag, Pd-loaded Bi_2WO_6 and its photocatalytic activities. *Adv. Mater. Res.* 2012, 518, 833–836.

[23] Li YL, Liu YM, Wang JS, Uchaker E, Zhang Q, Sun S, Huang Y, Li J, Cao G. Titanium alkoxide induced BiOBr-Bi_2WO_6 mesoporous nanosheet composites with much enhanced photocatalytic activity. *J. Mater. Chem. A* 2013, 1, 7949–7956.

[24] Gao E, Wang WZ, Shang M, Xu JH. Synthesis and enhanced photocatalytic performance of graphene-Bi_2WO_6 composite. *Phys. Chem. Chem. Phys.* 2011, 13, 2887–2893.

[25] Huang HW, Liu K, Chen K, Zhang YL, Zhang YH, Wang S. Ce and F comodification on the crystal structure and enhanced photocatalytic activity of Bi_2WO_6 photocatalyst under visible light irradiation. *J. Phys. Chem. C* 2014, 118, 14379–14387.

[26] Zeng C, Hua YM, Guo YX, Zhang TR, Dong F, Du X, Zhang YH, Huang HW. Achieving tunable photocatalytic activity enhancement by elaborately engineering composition-adjustable polynary heterojunctions photocatalysts. *Appl. Catal. B-Environ.* 2016, 194, 62–73.

[27] Huang HW, Li XW, Wang JJ, Dong F, Chu PK, Zhang TR, Zhang YH. Anionic group self-doping as a promising strategy: band-gap engineering and multi-functional applications of high-performance CO_3^{2-}-doped $Bi_2O_2CO_3$. *ACS Catal.* 2015, 5, 4094–4103.

[28] Zeng C, Hu YM, Huang HW. $BiOBr_{0.75}I_{0.25}$/$BiOIO_3$ as a novel heterojunctional photocatalyst with superior visible-light-driven photocatalytic activity in removing diverse industrial pollutants. *ACS Sustain. Chem. Eng.* 2017, 5, 3897–3905.

[29] Geim AK, Novoselov KS. Detection of individual gas molecules adsorbed on graphene. *Nat. mater.* 2007, 6, 183–191.

[30] Allen MJ, Tung VC, Kaner RB. Honeycomb carbon: a review of graphene. *Chem. Rev.* 2010, 110, 132–145.

[31] Allen MJ, Tung VC, Kaner RB. Enhanced photocatalytic performance of Bi_2WO_6 by graphene supporter as charge transfer channel. *Sep. Purif. Technol.* 2012, 86, 98–105.

[32] Sun ZH, Guo JJ, Zhu SM, Mao L, Ma J, Zhang D. A high-performance Bi_2WO_6-graphene photocatalyst for visible light-induced H_2 and O_2 generation. Nanoscale 2014, 6, 2186–2193.

[33] Xu JJ, Ao YH, Chen MD. A simple method for the preparation of Bi_2WO_6-reduced graphene oxide with enhanced photocatalytic activity under visible light irradiation. *Mater. Lett.* 2013, 92, 126–128.

[34] Sun SM, Wang WZ, Ling Zhang L. Bi_2WO_6 quantum dots decorated reduced graphene oxide. *J. Phys. Chem. C* 2013, 117, 9113–9120.

[35] Lv H, Liu YM, Hu JY, Li ZJ, Lu Y. Ionic liquid-assisted hydrothermal synthesis of Bi_2WO_6-reduced graphene oxide composites with enhanced photocatalytic activity. *RSC Adv.* 2014, 4, 63238–63245.

[36] Yang J, Wang XH, Zhao XL, Dai J, Mo S. Synthesis of uniform Bi_2WO_6-reduced graphene oxide nanocomposites with significantly enhanced photocatalytic reduction activity. *J. Phys. Chem.* C 2015, 119, 3068–3078.

[37] Szabo T, Berkesi O, Forgo P, Josepovits K, Sanakis Y, Petridis D, Dékány I. Evolution of surface functional groups in a series of progressively oxidized graphite oxides. *Chem. Mater.* 2006, 18, 2740–2749.

[38] Zhang H, Lv XJ, Li YM, Wang Y, Li J. P25-graphene composite as a high performance photocatalyst. *ACS* Nano 2010, 4, 380–386.

[39] Yang MQ, Weng B, Xu YJ. Improving the visible light photoactivity of In_2S_3-graphene nanocomposite via a simple surface charge modification approach. Langmuir 2013, 29, 10549–10558.

[40] Wang J, Hernandez Y, Lotya M, Coleman JN, Blau WJ. Broadband nonlinear optical response of graphene dispersions. *Adv. Mater.* 2009, 21, 2430–2435.

[41] Zhang LS, Wang WZ, Zhou L, Xu HL. Bi_2WO_6 nano- and micro-structures: shape control and associated visible-light-driven photocatalytic activities. Small 2007, 3, 1618–1625.

[42] Tian J, Sang YH, Yu GW, Jiang HD, Mu XN, Liu HA. Bi_2WO_6-based hybrid photocatalyst with broad spectrum photocatalytic properties under UV, visible, and near-infrared irradiation. *Adv. Mater.* 2013, 25, 5075–5080.

[43] Liu H, Cao WR, Su Y, Wang Y, Wang XH. Synthesis, characterization and photocatalytic performance of novel visible-light-induced Ag/BiOI. *Appl. Catal. B* 2012, 111, 271–279.

[44] Geng J, Lu DJ, Zhu JJ, Chen HY. Antimony (III)-doped $PbWO_4$ crystals with enhanced photoluminescence via a shape-controlled sonochemical route. *J. Phys. Chem.* B 2006, 110, 1377–1385.

[45] Cui ZK, Zeng DW, Tang TT, Liu J, Xie CS. Processing-structure-property relationships of Bi_2WO_6 nanostructures as visible-light-driven photocatalyst. *J. Hazard. Mater.* 2010, 183, 211–217.

[46] Xu CX, Wei X, Ren ZH, Wang Y, Xu G, Shen G, Han GR. Solvothermal preparation of Bi_2WO_6 nanocrystals with improved visible light photocatalytic activity. *Mater. Lett.* 2009, 63, 2194–2197.

[47] Wang XJ, Wang Q, Li FT, Yang WY, Zhao Y, Hao YJ, Liu SJ. Novel BiOCl-C_3N_4 heterojunction photocatalysts: in situ preparation via an ionic-liquid-assisted solvent-thermal route and their visible-light photocatalytic activities. *Chem. Eng. J.* 2013, 234, 361–371.

[48] Zhao W, Chen C, Li X, Zhao J, Hidaka H, Serpone N. Photodegradation of sulforhodamine-B dye in platinized titania dispersions under visible light irradiation: influence of platinum as a functional Co-catalyst. *J. Phys. Chem. B* 2002, 106, 5022–5028.

Supplemental Material: The online version of this article offers supplementary material (https://doi.org/10.1515/ntrev-2017-0153).

Supporting Information

As shown in Figure S1a, the characteristic diffraction peak (002) of the original graphite appears at around $2\theta = 26.5^0$, and the interplanar spacing is about 0.34 nm. After oxidation, this diffraction peak shifted to a lower angle around 11^0 (Figure S1b). There are no other obvious peaks can be detected, it indicates that the graphite completely almost is oxidized to GO.

Fig. S1. XRD patterns of the graphite and as-synthesized GO samples. (a) Graphite; (b) GO.